Electrochimica Acta 108 (2013) 575–582

Contents lists available at ScienceDirect

Electrochimica Acta

journal homepage: www.elsevier.com/locate/electacta

Impedance analysis of $Na_{0.44}MnO_2$ positive electrode for reversible sodium batteries in organic electrolyte

Riccardo Ruffo[a,*], Reza Fathi[a], Dong Jun Kim[b], Young Hwa Jung[b], Claudio M. Mari[a], Do Kyung Kim[b]

[a] Department of Materials Science, Università degli Studi di Milano-Bicocca, via Cozzi 53, 20125 Milano, Italy
[b] Department of Materials Science and Engineering, Korea Advanced Institute of Science and Technology (KAIST), 291 Daehak-ro, Yuseong-gu, Daejeon 305-701, Republic of Korea

ARTICLE INFO

Article history:
Received 18 February 2013
Received in revised form 5 June 2013
Accepted 1 July 2013
Available online 12 July 2013

Keywords:
Sodium manganese oxide
Cathode material
Sodium ion batteries
Impedance spectroscopy
Solid state diffusion

ABSTRACT

$Na_{0.44}MnO_2$ (NMO) is one of the most promising positive electrode materials for the development of sodium ion secondary batteries. In this work, a NMO orthorhombic compound was prepared by a soft chemistry modified Pechini method and characterized. The material exhibits a good discharge capacity (about 110 mAh/g) at low current rate (11 mA/g, C/25) which decreases to 65 mAh/g at high rate (275 mA/g, 1C). The electrochemical behavior was investigated by the extensive use of electrochemical impedance spectroscopy analysis. It was observed that the kinetic limitations are mainly due to the low diffusion coefficient of Na^+ ions in the structure (in the range $10^{-13}/10^{-14}$ cm^2/s) and to the high values of the surface resistance which is the sum of two contributes attributed to the charge transfer process and the presence of a passivating layer. The diffusion coefficient as well as the charge transfer resistance depends on the sodium amount in the electrode.

1. Introduction

With the increase in the commercialization of hybrid electrical vehicles and electrical vehicles powered by lithium ion batteries, the demand of lithium raw material might become astronomical in the near future [1]. This aspect will imply also geopolitical issues as lithium is becoming a strategic material [2]. A possible solution is the development of different battery systems and, in this framework, there is growing interest in the sodium based secondary batteries, which were already investigated at the early stage of lithium ion technology but after the commercialization of the first rocking chair battery were almost abandoned. In fact, there has been an exponential growth in the number of papers published about the development of electrode materials for sodium ion batteries in the last two years.

At present, the most promising sodium systems use a transition metal oxide and hard carbon as positive and negative electrode, respectively. In this configuration, considering the material specific capacity and the discharge profiles, the battery could be reasonably able to display an energy density of about 70–80% of lithium analogous with unexplored power density. However, several polycrystalline compounds show a lower diffusivity barrier for Na^+ compared to Li^+ homologous structures [3].

Among the oxide materials, different phases have been proposed like $NaCrO_2$ [4], Na_xCoO_2 [5–7], Na_xMnO_2 [8–13], and $Na_xMn_{0.5}Fe_{0.5}O_2$ [14] showing capacity about 100–150 mAh/g in the potential range from 2.0 to 4.0 V vs. metallic sodium with good kinetics. In particular, $Na_{0.44}MnO_2$ (NMO) has received significant attention due to the presence of the relative inexpensive and environmental friendly Mn in the structure. In addition, NMO can be prepared via facile synthetic methods such as hydrothermal [9,10], solid-state [8], sol–gel [11], polymer–pyrolysis [12], and combustion processes [11]. However, up to now the poor rate capability of NMO restricts its practical applications in room temperature sodium systems. In fact, Sauvage et al. [8] showed that NMO based electrodes cycled at current higher than C/20 rate displayed a sharp decrease in the delivered capacity. More recently, Cao et al. [12] and Hosono et al. [13] reported improved rate capability using NMO nanowires, which provided a shorter diffusion path for sodium insertion/deinsertion. Nevertheless, the improved rate-capability is still lower respect to morphology optimized lithium systems. In addition, the sodium intercalation in NMO involves multi-transition steps, which indicates complex structural behavior [15]. Therefore, detailed analysis of the kinetic behavior of NMO based electrodes is needed to exploit its successful use in sodium ion batteries.

A useful tool to study the electrochemical kinetic behavior of electrode material is impedance spectroscopy (IS). In the case of lithium-ion battery components, this approach has been widely used; detailed models exist to take into account the different

* Corresponding author. Tel.: +39 02 64485153; fax: +39 02 64485400.
E-mail address: riccardo.ruffo@unimib.it (R. Ruffo).

0013-4686/$ – see front matter © 2013 Elsevier Ltd. All rights reserved.
http://dx.doi.org/10.1016/j.electacta.2013.07.009

physical, chemical, and electrochemical contributions to the total electrode impedance of the cell or of one single element (positive electrode, negative electrode, or electrolyte). This approach has been extensively discussed by Barsoukov [16].

In the present work we describe the impedance behavior of NMO-based electrodes, obtained by a soft chemistry method, during the sodium ion intercalation and at different cycle numbers. The impedance responses are evaluated in terms of equivalent circuits, and the various contributions to the overall electrode resistance are analyzed both qualitatively and quantitatively.

2. Materials and methods

2.1. Preparation and characterization of $Na_{0.44}MnO_2$ sample

$Na_{0.44}MnO_2$ particles were prepared by a modified Pechini method starting from sodium carbonate and manganese acetate precursors, which were dissolved in DI water and then mixed with citric acid. The transparent solution was then gently heated to allow solvent evaporation and gel formation. The obtained gel was preheated to 300 °C to burn the organic binders. Finally, a thermal treatment at 800 °C in air for 9 h was performed to promote the sample crystallization.

The NMO crystal structure was characterized by X-ray diffractometer (Rigaku, Model D/MAX-RB, Japan). The morphology was confirmed by Field Emission Scanning Electron Microscope (Model XL30SFEG, Philips, The Netherlands) and Transmission Electron Microscope (Tecnai G2 F30. 300 kV, Philips, The Netherlands).

2.2. Electrochemical characterization

The electrochemical characterization was carried out using three electrode *T*-shaped Swagelok cells equipped with stainless steel current collectors. Active material electrodes were fabricated by mixing NMO active material (70%), PVDF binder (15%) and conductive carbon black (15%, Super P MMM Carbon). The mixture was dispersed in n-methyl-pyrrolidone (NMP) to obtain dense slurry which was then cast directly on the stainless steel current collector of the Swagelok cell and finally dried at 90 °C for 2 h. The active material load was around 2.5 mg/cm^2. Metallic sodium discs were pasted at the top of the two different current collectors, and they were used as reference and counter electrode, respectively. All the potentials are reported vs. the couple Na^+/Na. The small gap among the electrodes (around 1 mm) was filled with the electrolyte which was a solution of 1 M $NaClO_4$ (ACS reagent, Sigma–Aldrich) in propylene carbonate (Selectipur, Merck). The electrolyte salt was purified by crystallization from dioxane–water solution and the precipitate was then dried under vacuum at 150 °C. The propylene carbonate solvent was used as received. All the chemicals were stored in Ar filled glove box. The cell arrangement, avoiding the use of a separator, minimizes the number of materials used in cell assembling; thus the result is directly relatable to the material performances.

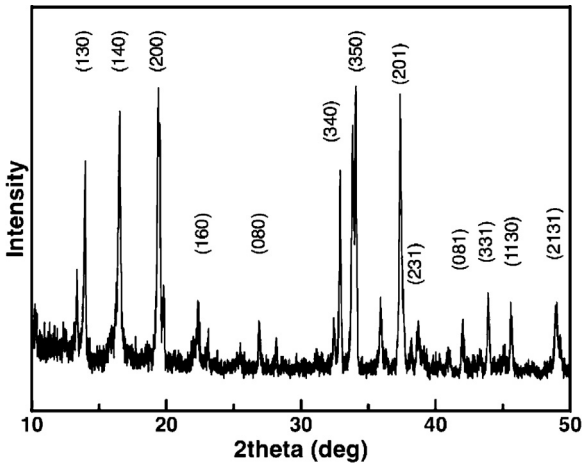

Fig. 1. XRD pattern of the synthesized NMO particles.

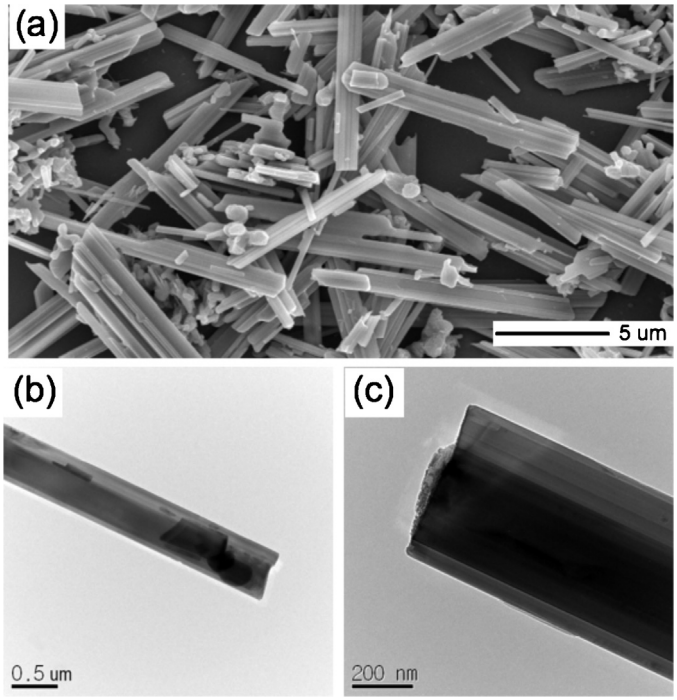

Fig. 2. Microstructures of the synthesized NMO particles observed by (a) SEM and (b and c) TEM.

The electrochemical characterization was carried out at room temperature using Biologic VMP3 multi-channel battery tester equipped with the Electrochemical Impedance Spectroscopy (EIS) board. Typical EIS experiments were performed at open circuit voltage (OCV) in the frequency range from 1×10^5 to 1×10^{-2} Hz under a DC stimulus of 10 mV after attaining the equilibrium conditions, i.e. until no variation of the OCV was observed.

3. Results and discussion

3.1. Powders structure and morphology

The X-ray pattern of the NMO powders prepared by the Pechini method is reported in Fig. 1. The lattice structure is orthorhombic and belongs to the *Pbam* space group, which corresponds to JCPDS card #27-0750. The pattern indicates a good crystallinity of the powders obtained by the solution precipitation method using a relatively short thermal treatment, compared to longer solid state reactions. All the Mn(IV) and half of the Mn(III) ions are present in octahedral sites, whereas the remaining Mn(III) ions are present in square-pyramidal sites. They form three-dimensional *S*-shaped tunnels, which allow sodium ions to be reversibly extracted/inserted and also small pentagonal tunnels containing non-extractable sodium ions [17]. Taking into account the structural aspects, the corresponding theoretical capacity is 121 mAh/g.

The morphology of the synthesized NMO powder is shown in Fig. 2. The use of a solution based preparation method allows to also the control the powder morphology. These conditions lead to rod-shaped NMO microparticles with typical dimensions of a few

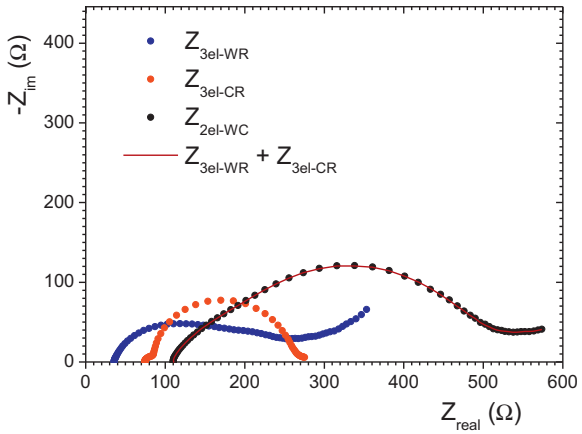

Fig. 3. Nyquist plots of the different cell arrangements. $Z_{3el\text{-}WR}$: impedance measured between the NMO/electrolyte and the Na/electrolyte interfaces using the other Na/electrolyte as counter electrode, $Z_{3el\text{-}CR}$: impedance measured between the two Na/electrolyte interfaces using the NMO/electrolyte as counter electrode, $Z_{2el\text{-}WC}$: impedance measured between the NMO/electrolyte and the Na/electrolyte in the classical two electrodes arrangement, $Z_{3el\text{-}WR} + Z_{3el\text{-}CR}$: algebraic sum of the impedances obtained in the three electrodes configurations.

μm in length, about 1 μm in width and several hundred nm in thickness.

3.2. EIS data validation

In order to be sure that the measured impedance would be directly related to the NMO/electrolyte interface without parasitic contributes, the three electrode Swagelok cell arrangement was chosen and validated by using three different cell configurations, two of them with three electrodes and one with two electrodes. In the first arrangement, the impedances of the NMO/electrolyte interface (working electrode, WE) was measured vs. the Na/electrolyte interface (reference electrode, RE) and the other Na/electrolyte interface (counter electrode, CE) was used to collect the induced current. This configuration will be indicated as $Z_{3el\text{-}WR}$ in the following. In the second arrangement with three electrodes, the impedance between the two Na/electrolyte interfaces (RE and CE) was measured using the NMO/electrolyte interface (WE) to collect the current, this configuration will be indicated as $Z_{3el\text{-}CR}$. Finally, the impedance between the WE and the CE was measured without the use of a third electrode in a classical two electrodes measurement and it will be indicated as $Z_{2el\text{-}WC}$. If the measurement is independent of the shape and position of the RE, the sum of the two three-electrode impedances ($Z_{3el\text{-}WR} + Z_{3el\text{-}CR}$) has to be similar to the two-electrode configuration $Z_{2el\text{-}WC}$ [18–20]. The impedance answers of all the three different configurations ($Z_{3el\text{-}WR}$, $Z_{3el\text{-}CR}$, and $Z_{2el\text{-}WC}$) are reported in Fig. 3 in terms of Nyquist plots. From the comparison it is clear that the impedance at the Na/electrolyte interfaces ($Z_{3el\text{-}CR}$) is not negligible, so the two electrode measurements ($Z_{2el\text{-}WC}$) cannot be used as representative of the working electrode impedance. Moreover, the $Z_{3el\text{-}WR} + Z_{3el\text{-}CR}$ sum differs from the $Z_{2el\text{-}WC}$ by less than 1% in the 1×10^4–1×10^{-2} Hz frequency range pointing out the validity of the chosen configuration. Stable and reproducible spectra were obtained in Swagelock cells with different samples.

3.3. First charge/discharge curve

EIS measurements were used to monitor the electrode impedance change as a function of the first cycle depth of discharge (DOD) and of the second cycle state of charge (SOC). To change the electrode charge we used galvanostatic pulses (11 mA/g, C/25) in

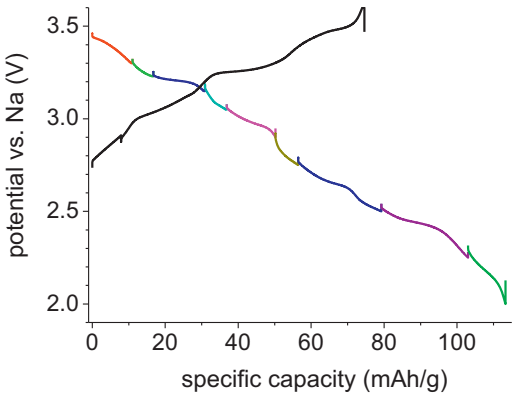

Fig. 4. Charge (black) and discharge step profile at 11 mA/g.

the potential range between 3.5 and 2.0 V, after a charging step at the same current rate. The first charge/discharge profile is reported in Fig. 4 and shows a series of potential drops due to complex compositional behavior of the Na_xMnO_2 material. In fact, it was already pointed out that the electrochemical insertion/deinsertion of sodium in the phase does not proceed through a single solid solution mechanism, but through several multiphase reactions [8]. In particular, four main reactions are present in the investigated compositional range, corresponding to potential drops at 3.2, 2.9, 2.6, and 2.4 V. Below this last potential, the potential profile appears to be related to the intercalation of Na^+ only in a single phase domain.

Typical Nyquist plots obtained at different DOD and SOC are reported in Fig. 5. At high frequencies (above 5×10^4 Hz), the spectrum is dominated by the sum of the contributions of the external cell connections, the electronic conduction between the substrate and the active material, and the ionic conduction through the electrolyte. Since the highest experimental frequency is too low to see inductance distortions in the spectra, these contributions appear as a pure resistive behavior (Z_{im} close to 0) and are dominated by the ionic conductivity of the electrolyte, which can be determined by the high frequency intercept of the real axis. No significant changes were observed in all the experiments. As the frequency decreases, a first arc appears in the spectrum followed by a second semicircle and a portion of straight line at the lowest frequencies. In this frequency range, the impedance of lithium ion battery electrode is due to the complex electrochemical reactions taking place at the interfaces. This kind of answer can usually be attributed to three different reasons: the formation of a passivating layer (often called Solid Electrolyte Interface, SEI) on the active particle surface, the charge transfer process coupled with the double layer capacitance and the solid state diffusion in the active particle. Several equivalent circuits can be used to describe the situation, from the simple Randles-type circuit to more complex systems built by several sub-circuits. This ambiguous situation is also complicated by the fact that several equivalent circuits have the same mathematic representation. In any case, the impedance of lithium-ion battery electrodes is usually modeled by considering all the chemical–physical processes in series, each of them represented by a sub-circuit element [16]. In this case, the electric equivalent circuit (see onset of Fig. 6) was built by the combination of three elements: one serial resistance (R_{ser}), one parallel RC circuit taking into account the sodium ionic conductivity in the SEI layer (R_{SEI}, C_{SEI}), and one Randels type circuit describing the charge transfer process (R_{ct}), the double layer capacity (C_{dl}) and the diffusion element into the particles bulk (Z_D). Due to the electrode roughness, the ideal capacitance elements have been replaced by the frequency depended Constant Phase Elements (CPE), whose frequency dependent parameter (ω^n) is in all the cases >0.75 ($n = 1$

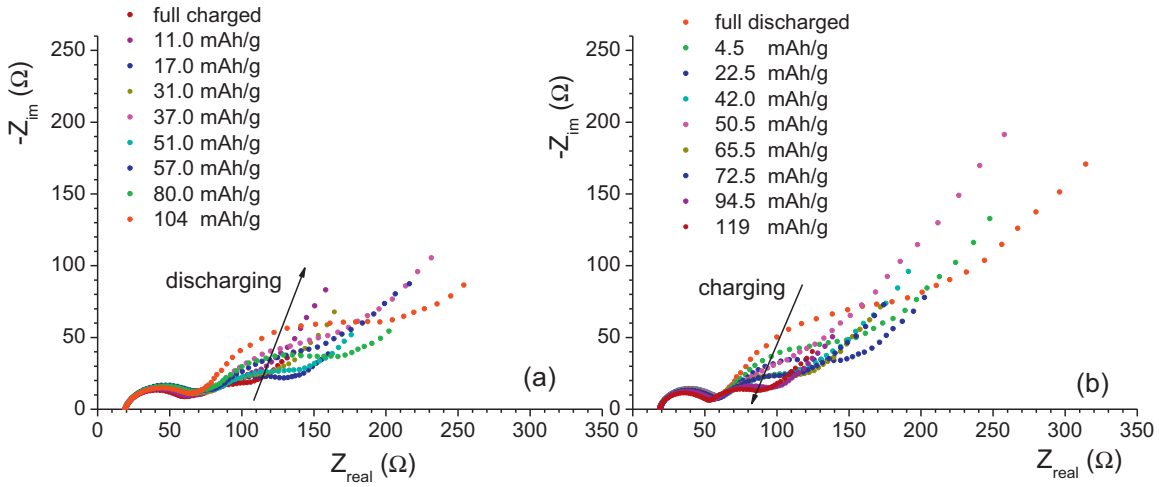

Fig. 5. Nyquist plots of the NMO electrode at different DODs (a) and SOCs (b).

for an ideal capacity). By the use of this equivalent circuit it was possible to fit the experimental spectra with reasonable agreement.

The change of both the SEI and the charge transfer resistances is reported in Fig. 6 as a function of the DOD and the SOC. The presence of SEI layer on the surface of cathode materials for sodium ion batteries has been suggested recently [21], moreover a large irreversibility of the first cycle process in generally observed on oxides [6]. As it is possible to observe, the SEI resistance slightly changes with the electrode capacity, and it may be considered as constant during the material charge and discharge; the particle surface forms a stable layer, which does not change its electrical properties with the potential or the phase composition. Such observation is also confirmed by the capacitance value, which is constant (about 1×10^{-6} F/cm^2) for all the measurements. On the contrary, the charge transfer resistance increases with the sodium amount in the phase. In particular, the major changes are in proximity of new phase formations, at potential between 2.9 and 2.6 V and below 2.4 V, where the resistance value becomes almost double the initial one. Since the structural differences among the phases are almost negligible [8], the increase of the charge transfer resistance during discharging may be attributed to the increased sodium amount in the phase. The double layer capacitances at the interface particle/SEI are in the range of 1×10^{-4} F/cm^2.

At the lowest frequencies (below 1 Hz), the contribution of the solid-state diffusion is present (Z_D in the equivalent circuit of Fig. 6), i.e. Na ions moving into the bulk of active particle material. In this case, the presence of the metallic current collector blocks the diffusion of ions at the inner interface (the stainless steel current collector does not alloy with Na). The diffusion process should be represented by the semi-infinite diffusion line, which corresponds to the tangent-hyperbolic function (T), widely discussed in the literature [22–24]. The representation of T in the Nyquist plot is usually a diffusive Warburg segment at 45°, followed by the vertical capacitive line at the lowest frequencies. However, the explored frequency range may not be enough to appreciate the whole element, and only the Warburg part of T can be seen in all the spectra as in the case of Fig. 5, where the lowest frequency limit (1×10^{-2} Hz) is too high to see the capacitive limit. These spectra can be successfully fitted by using the Warburg element as diffusive element ($Z_D = W$). To confirm the presence of the semi-infinite diffusion line, we have also obtained one spectrum (at DOD = 104 mAh/g) until 1×10^{-4} Hz (Fig. 7). In this case, the measurement requires several hours and the external cell conditions have to be carefully controlled (constant temperature). As expected, at a frequency below 1×10^{-2} Hz the straight line bends out toward a vertical line, even if the limiting capacity behavior does not ever appear. For this reason, the spectrum was modeled by the usual equivalent circuit in which the Modified Restricted Diffusion Element was used as Z_D. This element is very similar to the T, but includes a dispersion parameter to

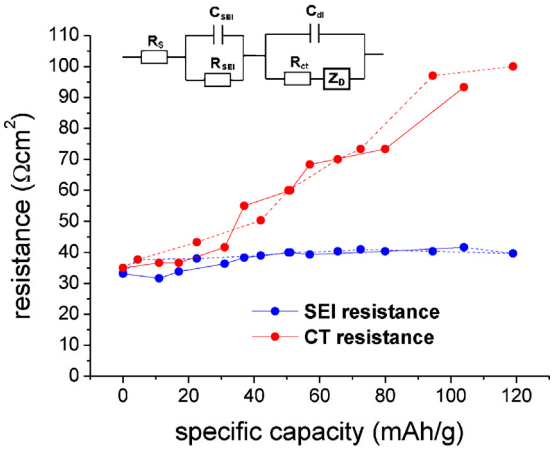

Fig. 6. Charge transfer and SEI resistances as a function of the specific capacity measured during discharge (continuous line) and charge (dashed line).

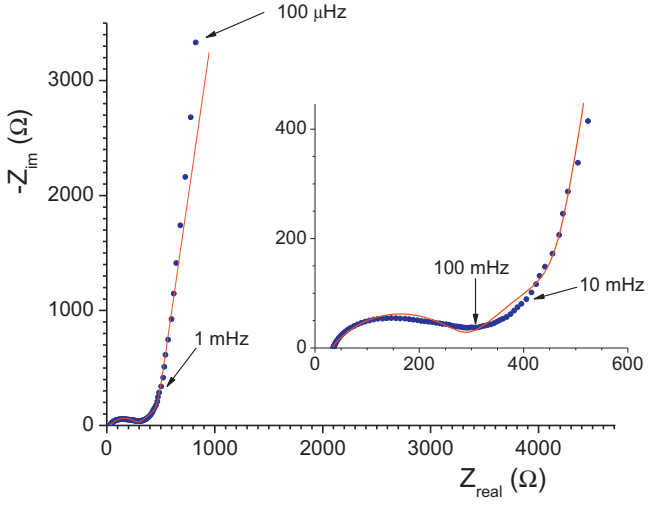

Fig. 7. Nyquist plot at 104 mAh/g in the frequency range 1×10^5–1×10^{-4} Hz.

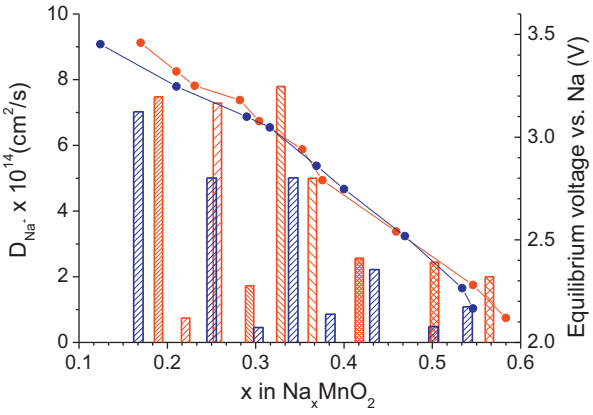

Fig. 8. Average sodium diffusion coefficients during discharge (red bars) and charge (blue bars) as a function of the Na^+ composition. Equilibrium potentials are also reported on the right axis. (For interpretation of the references to color in text, the reader is referred to the web version of this article.)

take into account a more complex frequency dependence, as in the case of the difference between the ideal capacitance and the CPE [25]. The result of the fit is reported in Fig. 7 as a red line and, in this case, the resistance associated with the diffusion process is around 500 Ω, while those of SEI layer and charge transfer resistance are 120 and 170 Ω, respectively.

The sodium ion solid-state diffusion process can be better characterized if the diffusion coefficient (D_{Na+}) is calculated. Due to the hard experimental conditions to obtain stable and reproducible low frequency data and the complex modeling, we have calculated the sodium ion diffusion coefficient using the Warburg elements obtained from the spectra in Fig. 5. In fact, Ho et al. [23] demonstrated that the Warburg impedance arising from the chemical diffusion in solid state is expressed by the following equations:

$$Z_W = Z_D\,\omega^{1/2}$$

$$Z_D = V_m(dE/dx)/(zFD^{1/2}A)$$

where Z_D is the pre-exponential factor of the Warburg impedance, ω is the a.c. frequency, V_m is the molar volume, F is the Faraday constant, A is the electrode area, and (dE/dx) is the slope of equilibrium electrode potential vs. composition. The Z_D expression can be used to calculate D once all the other parameters are known [26,27]. In the present case, $V_m = 22.85\ cm^3/mol$, $A = 2.45\ m^2/g$ as determined using BET method, Z_D is obtained from EIS data in the frequency range above 1×10^{-2} Hz, and (dE/dx) was measured at the end of each charging/discharging step after waiting for equilibrium conditions. The reported D is thus the average value in the corresponding composition range. Moreover, diffusion coefficients were calculated based on the assumption that the whole surface area of the active material is wet by the electrolyte in spite of the presence of binder and carbon additive materials. Also, the molar volume of the active material is assumed to be constant throughout the intercalation/extraction process despite the changes in the Na ion composition within the active material during these processes. Hence, the diffusion coefficient values presented in this work are apparent values whose relative errors have been estimated as ±10%. The obtained D_{Na+} values are reported in Fig. 8 and they change with the voltage/composition of the electrode. Good agreement has been observed for the charge and discharge process. In particular, the composition range can be divided into two domains for x higher or lower than 0.35 in Na_xMnO_2. The highest values for the diffusion coefficient are in the sodium poor composition range ($x < 0.35$), where D_{Na+} shows also sudden drops of one order of magnitude during phase transformations ($0.21 < x < 0.23$ and $0.28 < x < 0.30$). On the contrary, the sodium rich portion of the graph is characterized by lower D_{Na+} values, which decrease with the increase of the sodium amount. Thus, both the structural rearrangements and the sodium composition control the diffusion kinetic in the phase.

3.4. Evolution of impedance with temperature

To better identify the different processes involved, impedance measurements were also performed in the temperature range 10–70 °C. Two points of the potential/capacity profile were explored at equilibrium values of 3.20 V (corresponding to 67 mAh/g) and 2.43 V (93 mAh/g) to get activation energies at both low and high sodium concentration, respectively. Fig. 9 reports the spectra evolution as a function of the temperature at the two potentials. The Arrhenius plots corresponding to the different kind of processes (Fig. 10) were calculated from the resistances and the Warburg element of the electrical circuit reported in Fig. 6. In particular, the exchange current density (i_0) of the electrochemical reaction was calculated from the charge transfer resistance and the BET surface area. The i_0 values range from 1 to 10 μA/cm^2 at low and high temperature, respectively, with activation energies of 0.28 ± 0.04 eV (low [Na^+]) 0.30 ± 0.07 eV (high [Na^+], Fig. 10a). These values are slightly higher than the corresponding activation energies in lithium metal oxides [28] and are comparable to those of lithium metal phosphate [29]. The resistances attributed to the SEI process show a slight steep slope and low activation energies

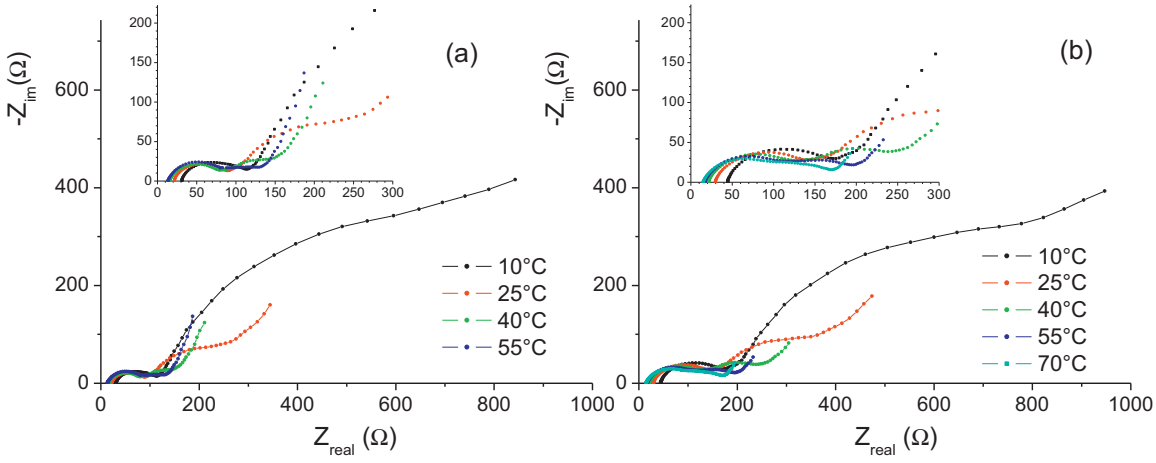

Fig. 9. Nyquist plots at different temperature measured at the equilibrium potential of 3.20 V (a) and 2.43 V (b).

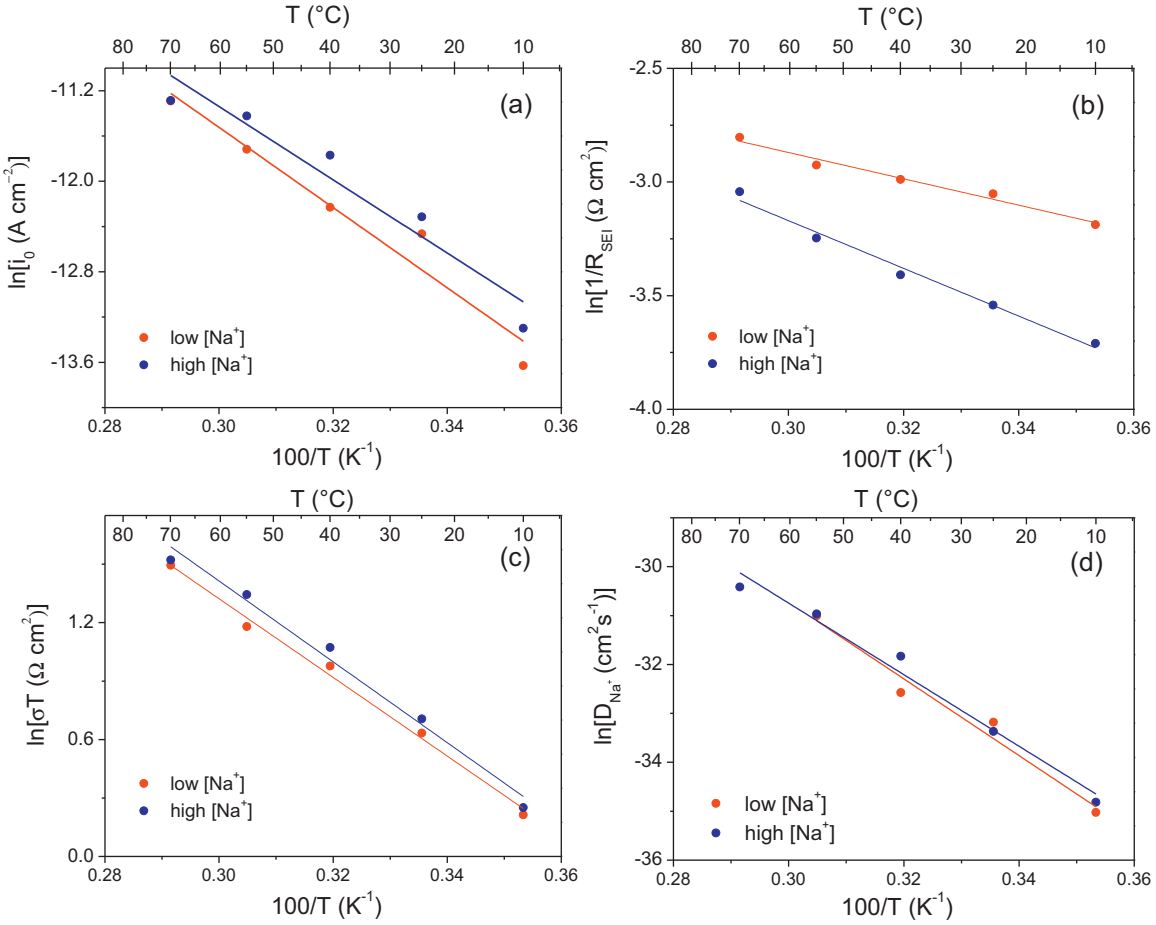

Fig. 10. Arrhenius plots obtained for (a) the charge transfer exchange current density (i_0); (b) the resistance associate to the SEI presence; (c) the ionic conductivity of the electrolyte (σ); (d) the diffusion coefficient (D_{Na+}).

(0.09 ± 0.01 eV and 0.05 ± 0.005 eV at low and high [Na^+], respectively, see Fig. 10b). To our knowledge do not exist other data to compare with, however this behavior may be attribute to diffusion in the polymeric film formed on the particle surface. The ionic conductivity of the electrolyte (σ) was obtained from the serial resistance. The values at 25 °C (around 6 mS/cm) are in very good agreement with that reported from Ponrouch et al. [30] and the activation energies are also independent on the DOD (0.17 ± 0.2 eV) and in agreement with that of the ionic conductivity of similar lithium ion electrolytes [31]. Thus, the serial resistance is mainly related to the ionic conductivity of the electrolyte. Finally, the activation energy for the diffusion process in NMO has the same value (0.63 ± 0.05 eV) at the two sodium ion concentration and it is similar to those reported by Kim et al. [3] for diffusion barrier in sodium metal oxides.

3.5. Cycling properties

The results of the impedance analysis clearly show that at elevated DOD or low SOC the charge transfer resistance increases, while at the same time the diffusion coefficient decreases. Both these aspects contribute to slowing down the kinetic of the electrode reaction and may affect the electrode behavior upon cycling. To better clarify this aspect, we have cycled the NMO electrode for 30 times at low current (11 mA/g) between 2.0 and 3.5 V and measured the electrode impedance at the end of some selected cycles (1, 2, 5, 10, 20, and 30). At this rate, the NMO electrode was initially able to supply most of the expected capacity value (121 mAh/g) considering all the mobile Na^+ ions; then the charge decreases upon cycling and stabilizes after 20 cycles at 105 mAh/g (see Fig. 11). The corresponding Coulomb efficiency is in the range of 95/97%. This behavior can be better understood looking at the change in the surface resistance values vs. the number of the cycles. As reported in Fig. 12, the SEI resistance is basically unchanged upon cycling, while the charge transfer resistance increases after 20 cycles at a value which is almost double that of the initial one. To understand the kinetic limits of the system, after the first 30 cycles at low

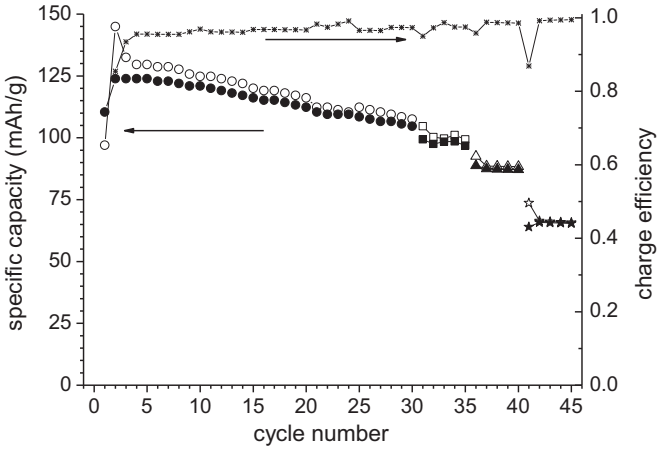

Fig. 11. Charge (empty symbol) and discharge (full symbol) capacity and Coulomb efficiency of NMO electrode cycled at different current densities: 11.0 mA/g (circles), 27.5 mA/g (squares), 55 mA/g (triangles), and 275 mA/g (stars).

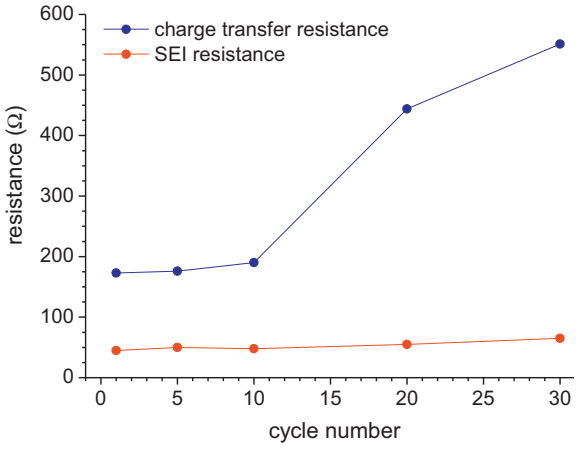

Fig. 12. Evolution of the charge transfer and SEI resistances (end of discharge) with the cycling.

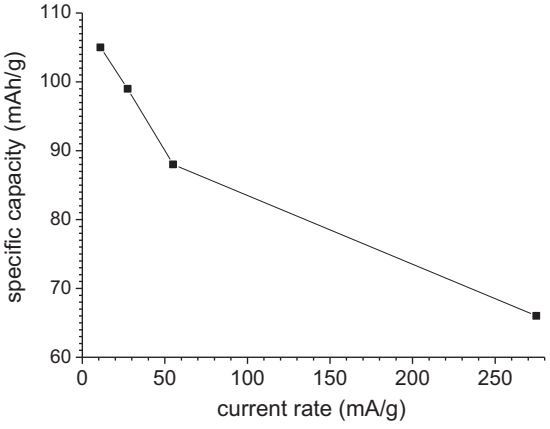

Fig. 13. Specific discharge capacity as a function of the current rate.

current, we progressively increased the current every 5 cycles to 27.5 mA/g, 55.0 mA/g, and 275 mA/g. At intermediate currents (27.5 and 55.0 mA/g) the electrode is still able to supply a good discharge capacity (100 and 90 mAh/g, respectively), while at the highest rate a lower capacity value was observed (65 mAh/g) (Figs. 11 and 13). In the measurements performed at a higher rate the charge efficiency increases, indicating the presence of one side reaction during the anodic process: the less the time the system remains at oxidative potentials, the higher the efficiency.

4. Conclusions

The NMO phase prepared by the modified Pechini method exhibits a discharge capacity of about 110 mAh/g at low current rate (11 mA/g), which decreases to 65 mAh/g at high rate (275 mA/g). From the electrochemical impedance analysis (EIS), an elegant method to analyze the kinetic behavior of electrode materials, it is clear that both the surface resistance and the ion diffusion in the solid phase play a role in limiting the material performances, while the contribute of the electrolyte conductivity is negligible. EIS measurements performed at different temperatures allowed the determination of the activation energies whose values confirmed the interpretation of the various processes. There are two chemical/physics processes, which contribute to the overall surface resistance: the well known charge transfer resistance and the presence of a passivating layer (SEI) on the particle surface. Only the former (charge transfer resistance) depends on both the electrode charge state and the cycling process, while the latter (SEI contribute) remains almost the same.

In the end it is necessary to emphasize that only the measurements carried out at a very low frequency are able to display the tangent-hyperbolic behavior of the semi-infinite diffusion impedance, which is characterized by a resistance value (500 Ω), similar to those observed for the electrode surface (300 Ω).

Acknowledgements

The authors are grateful to the Fondazione Cariplo for their funding (contract 2011-0312, “Give sodium a chance: Investigation of nanostructured mixed Na oxides as electrode materials for energy storage”). This work was also supported by Program to Solve Climate Changes (NRF-2010-C1AAA001-2010-0029031) through the National Research Foundation of Korea (NRF) funded by the Ministry of Education, Science and Technology.

References

[1] J.M. Tarascon, Is lithium the new gold? Nat. Chem. 10 (2010) 510.
[2] O. Ebgue, Study outlines supply chain challenges for lithium future, in: ScienceDaily, Missouri University of Science and Technology, 2012 (retrieved 24.10.12) http://www.sciencedaily.com-/releases/2012/09/120921140112.htm
[3] S. Kim, X. Ma, S. Ping Ong, G. Ceder, A comparison of destabilization mechanisms of the layered $NaxMO_2$ and $LixMO_2$ compounds upon alkali de-intercalation, Phys. Chem. Chem. Phys. 14 (2012) 15571.
[4] S. Komaba, C. Takei, T. Nakayama, A. Ogata, N. Yabuuchi, Electrochemical intercalation activity of layered $NaCrO_2$ vs. $LiCrO_2$, Electrochem. Commun. 12 (3) (2010) 355.
[5] C. Delmas, J.-J. Braconnier, C. Fouassier, P. Hagenmuller, Electrochemical intercalation of sodium in $NaxCoO_2$ bronzes, Solid State Ionics 3 (1981) 165.
[6] R. Berthelot, D. Carlier, C. Delmas, Electrochemical investigation of the P_2–$NaxCoO_2$ phase diagram, Nat. Mater. 10 (2011) 74.
[7] M. D'Arienzo, R. Ruffo, R. Scotti, F. Morazzoni, C.M. Mari, Layered $Na_{0.71}CoO_2$: a powerful candidate for viable and high performance Na-batteries, Phys. Chem. Chem. Phys. 14 (2012) 5945.
[8] F. Sauvage, L. Laffont, J.M. Tarascon, E. Baudrin, Study of the insertion/deinsertion mechanism of sodium into $Na_{0.44}MnO_2$, Inorg. Chem. 46 (2007) 3289.
[9] Y. Li, Y. Wu, Formation of $Na_{0.44}MnO_2$ nanowires via stress-induced splitting of birnessite nanosheets, Nano Res. 2 (2009) 54.
[10] E. Hosono, H. Matsuda, I. Honma, S. Fujihara, M. Ichihara, H. Zhou, Synthesis of single crystalline electro-conductive $Na_{0.44}MnO_2$ nanowires with high aspect ratio for the fast charge–discharge Li ion battery, J. Power Sources 182 (2008) 349.
[11] M.M. Doeff, T.J. Richardson, J. Hollingsworth, C.-W. Yuan, M. Gonzales, Synthesis and characterization of a copper-substituted manganese oxide with the $Na_{0.44}MnO_2$ structure, J. Power Sources 112 (2002) 294.
[12] Y. Cao, L. Xiao, W. Wang, D. Choi, Z. Nie, J. Yu, L.V. Saraf, Z. Yang, J. Liu, Reversible sodium ion insertion in single crystalline manganese oxide nanowires with long cycle life, Adv. Mater. 23 (2011) 3155.
[13] E. Hosono, T. Saito, J. Hoshino, M. Okubo, Y. Saito, D. Nishio-Hamane, T. Kudo, H. Zhou, High power Na-ion rechargeable battery with single-crystalline $Na_{0.44}MnO_2$ nanowire electrode, J. Power Sources 217 (2012) 43.
[14] N. Yabuuchi, M. Kajiyama, J. Iwatate, H. Nishikawa, S. Hitomi, R. Okuyama, R. Usui, Y. Yamada, S. Komaba, P_2-type $Nax[Fe_{1/2}Mn_{1/2}]O_2$ made from earth-abundant elements for rechargeable Na batteries, Nat. Mater. 11 (2012) 512.
[15] H. Kim, D.J. Kim, D.-H. Seo, M.S. Yeom, K. Kang, D.K. Kim, Y. Jung, Ab initio study of the sodium intercalation and intermediate phases in $Na_{0.44}MnO_2$ for sodium-ion battery, Chem. Mater. 24 (2012) 1205.
[16] E. Barsoukov, in: E. Barsoukov, J.R. Macdonald (Eds.), Impedance Spectroscopy: Theory, Experiment, and Applications, John Wiley and Sons Inc., Hoboken, NJ, 2005, pp. 444–457, 462.
[17] I. Kruk, P. Zajdel, W. van Beek, I. Bakaimi, A. Lappas, C. Stock, M.A. Green, Coupled commensurate cation and charge modulation in the tunneled structure, $Na_{0.40(2)}MnO_2$, J. Am. Chem. Soc. 133 (2011) 13950.
[18] S. Leroy, F. Blanchard, R. Dedryvere, H. Martinez, B. Carre, D. Lemordant, D. Gonbeau, Surface film formation on a graphite electrode in Li-ion batteries: AFM and XPS study, Surf. Interface Anal. 37 (2005) 773.
[19] E. Barsoukov, J.H. Kim, C.O. Yoon, H. Lee, Kinetics of lithium intercalation into carbon anodes: in situ impedance investigation of thickness and potential dependence, Solid State Ionics 116 (1999) 249.
[20] R. Ruffo, S.S. Hong, C.K. Chan, R.A. Huggins, Y. Cui, Impedance analysis of silicon nanowire Lithium ion battery anodes, J. Phys. Chem. C 113 (2009) 11390.
[21] K.-H. Ha, S.H. Woo, D. Mok, N.-S. Choi, Y. Park, S.M. Oh, Y. Kim, J. Kim, J. Lee, L.F. Nazar, K.T. Lee, Na_4-αM_2+$\alpha/2(P_2O_7)_2$ ($2/3 \leq \alpha \leq 7/8$, M = Fe, $Fe_{0.5}Mn_{0.5}$, Mn): A promising sodium ion cathode for Na-ion batteries, Adv. Energy Mater. 3 (6) (2013) 770, http://dx.doi.org/10.1002/aenm.201200825.

[22] M. Dollé, F. Orsini, A.S. Gozdz, J.M. Tarascon, Development of reliable three-electrode impedance measurements in plastic Li-ion batteries, J. Electrochem. Soc. 148 (8) (2001) A851.
[23] C. Ho, I.D. Raistrick, R.A. Huggins, Application of A-C techniques to the study of lithium diffusion in tungsten trioxide thin films, J. Electrochem. Soc. 127 (2) (1980) 343–350.
[24] C.J. Wen, C. Ho, B.A. Boukamp, I.D. Raistrick, W. Weppner, R.A. Huggins, Use of electrochemical methods to determine chemical-diffusion coefficients in alloys: application to 'LiAl', Int. Mater. Rev. 5 (1981) 253.
[25] Handbook of Electrochemical Impedance Spectroscopy, http://www.bio-logic.info/potentiostat/notesheis.html
[26] O. Yamada, M. Ishikawa, M. Morita, Charge/discharge cycling and impedance response of $LiMn_2O_4$ electrode in organic electrolyte solutions with different compositions, Electrochim. Acta 45 (2000) 2197.
[27] K.M. Shaju, G.V. Subba Rao, B.V.R. Chowdari, EIS and GITT studies on oxide cathodes, O_2-$Li_{(2/3)}+x(Co_{0.15}Mn_{0.85})O_2$ (x = 0 and 1/3), Electrochim. Acta 48 (2003) 2691.
[28] C.M. Julien, Lithium intercalated compounds: Charge transfer and related properties, Mater. Sci. Eng. R. 40 (2003) 47–102.
[29] M. Takahashi, S. Tobishima, K. Takei, Y. Sakurai, Reaction behavior of $LiFePO_4$ as a cathode material for rechargeable lithium batteries, Solid State Ionics 148 (2002) 283–289.
[30] A. Ponrouch, E. Marchante, M. Courty, J.-M. Tarascon, M.R. Palacin, In search of an optimized electrolyte for Na-ion batteries, Energy Environ. Sci. 5 (2012) 8572–8583.
[31] R. Ruffo, F. La Mantia, C. Wessells, R.A. Huggins, Y. Cui, Electrochemical characterization of $LiCoO_2$ as rechargeable electrode in aqueous $LiNO_3$ electrolyte, Solid State Ionics 192 (1) (2011) 289–292.